

Evaluation and Projection of Changes in Daily Maximum Wind Speed over China Based on CMIP6[©]

JINLIN ZHA,^{a,b} CHENG SHEN,^c JIAN WU,^a DEMING ZHAO,^b WENXUAN FAN,^a HUIPING JIANG,^{d,e}
AND TIANBAO ZHAO^a

^a Key Laboratory of Atmospheric Environment and Processes in the Boundary Layer over the Low-Latitude Plateau Region, Department of Atmospheric Science, Yunnan University, Kunming, China

^b CAS Key Laboratory of Regional Climate and Environment for Temperate East Asia, Institute of Atmospheric Physics, Chinese Academy of Sciences, Beijing, China

^c University of Gothenburg, Department of Earth Sciences–Regional Climate Group, Gothenburg, Sweden

^d International Research Center of Big Data for Sustainable Development Goals (CBAS), Beijing, China

^e CAS Key Laboratory of Digital Earth Science, Aerospace Information Research Institute (AIR), Chinese Academy of Sciences (CAS), Beijing, China

(Manuscript received 24 March 2022, in final form 31 October 2022)

ABSTRACT: Future changes in spatiotemporal features of the mean wind speed over China have been extensively reported, but future changes in the maximum wind speed, such as the daily maximum wind speed (DMWS), were rarely estimated. In this study, the performance of Coupled Model Intercomparison Project phase 6 (CMIP6) models in simulating the DMWS changes across China is evaluated, based on which the projection on DMWS is carried out under different shared socioeconomic pathways (SSPs). The observed DMWS shows a significant reduction during all four seasons, with the strongest decrease in spring and the weakest decrease in autumn. The DMWS increases from January to April and decreases from April to August. The spatiotemporal characteristics of the DMWS are captured by the multimodel ensemble of CMIP6; however, the reduction of DMWS in CMIP6 is weaker than those in observations. The performance of CMIP6 in simulating the future DMWS changes over China shows regional and seasonal discrepancies. The projected DMWS exhibits a reduction for all SSPs from 2021 to 2100, and the decreasing trend is increased accompanied by the strength in the forcing scenario. The lower-emission scenario likely avoids the long-term weakening of the DMWS. The effects of strength in forcing scenarios on the trends of DMWS are more significant than the DMWS climate state. The seasonal cycle of the projected DMWS under the different SSPs is consistent with the historical DMWS; however, the strength in the forcing scenario could induce enhanced variability in the month-to-month DMWS difference.

SIGNIFICANCE STATEMENT: Estimation and projection of daily maximum wind speed (DMWS) are crucial for many socioeconomic and environmental issues, as DMWS can induce damage to buildings and infrastructure and affect the air quality and frequency of dust storms, among many other aspects. Nevertheless, future changes in the DMWS have rarely been investigated in China. This paper suggests that the lower forcing scenario could effectively avoid the long-term reduction in DMWS. The seasonal cycle of the future DMWS is consistent with the historical DMWS; however, the stronger forcing scenario induces the strengthening of the month-to-month wind speed difference variability. This study provides a scientific basis for decision-makers to formulate policies to deal with climate change.

KEYWORDS: Wind; Climate change; Climate prediction; Greenhouse gases; Decadal variability; Trends

1. Introduction

Wind speed is a key component in the atmospheric circulation, partially governing the transfer of energy, water, and momentum between the land surface and lower atmosphere (Kim and Paik 2015), reflecting the impacts of both climate change and anthropogenic activities (Wu et al. 2018a). Information on wind speed changes provides theoretical insights into regional evapotranspiration (Liu et al. 2014), water cycle

(McVicar et al. 2012), visibility (Wang et al. 2017), air pollution (Y. Zhang et al. 2020), evaluation of wind energy (Tian et al. 2019; Pryor et al. 2020), and wind-induced natural disasters (Wu et al. 2020), among many aspects. Consequently, an investigation of the long-term changes in wind speed would therefore be helpful to the recognition of the effects of these processes (Wu et al. 2018a).

Historical changes in mean wind speed from a global scale to a regional scale have been extensively investigated in the last few decades (Vautard et al. 2010; McVicar et al. 2012; Dadaser-Celik and Cengiz 2014; Zeng et al. 2019). Meanwhile, the causes of changes in historical mean wind speed are also unraveled, including the effects of large-scale ocean–atmosphere circulations and surface roughness changes induced by land use and cover change and urbanization (McVicar et al. 2008; Malloy et al. 2015; Laapas and Venalainen 2018;

[©] Supplemental information related to this paper is available at the Journals Online website: <https://doi.org/10.1175/JCLI-D-22-0193.s1>.

Corresponding author: Deming Zhao, zhaodm@tea.ac.cn

Wu et al. 2018b). In China, changes in mean wind speed and the possible causes are also discussed and estimated (Guo et al. 2011; Li et al. 2018; Zhang and Wang 2020; Zha et al. 2017a, 2021a; Zhang et al. 2021). Apart from studies on the historical wind speed, the mean wind speed changes are also projected (Akinsanola et al. 2021; Deng et al. 2021), including in China (Chen et al. 2012; Jiang et al. 2017, 2018), especially since phase 5 of the Coupled Model Intercomparison Project (CMIP5) came into operation. The Coupled Model Intercomparison Project (CMIP) is used extensively to understand future climate changes (Wu et al. 2020; H. Chen et al. 2020). Many studies have employed CMIP datasets (e.g., CMIP3, CMIP5, and CMIP6) to analyze the spatiotemporal characteristics of mean wind speed across China, and almost all studies have pointed out that the mean wind speed could decrease over most regions of China in the future (Chen et al. 2012; Wu et al. 2020; Zha et al. 2020, 2021b).

Climate extremes have received increasing attention in recent years, as they are potentially more sensitive to change and more directly linked to natural disasters than median climate conditions (Yan et al. 2002). The reduction in mean wind speed is mainly dominated by the reduction in the number of extreme wind speed events [e.g., daily maximum wind speed (DMWS)], which has been confirmed in earlier studies (Xu et al. 2006; Guo et al. 2011). Spatiotemporal characteristics of the historical maximum wind speed at the regional scales have been studied. The regional and seasonal differences in DMWS climatology are considerable. For instance, the highest DMWS was found in spring and the lowest DMWS was found in summer across the United States (Klink 1999). Both the magnitude and frequency of maximum wind speed declined across majority of Australia, with a seasonality: significant negative trends in summer, spring, and autumn, and weak positive trends in winter (Azorin-Molina et al. 2021). Yan et al. (2002, 2006) discovered that the DMWS has increased over the ocean during winter but weakened over continental Europe during summer. The interannual variations in the DMWS showed a statistically significant 5% increase between 1959 and the early 1990s, followed by an apparent decrease (Hewston and Dorling 2011). The existing observational evidence on the signs of trends in DMWS under the changing climate is inconclusive (Azorin-Molina et al. 2021).

Compared to the mean wind speed, extreme wind speed changes, such as DMWS, have received only minimal attention over recent decades in China. Jiang et al. (2010) pointed out that the maximum wind speed displayed a declining trend of $-0.10 \text{ m s}^{-1} \text{ decade}^{-1}$ in China from 1956 to 2004, with the most rapid decline occurring in spring. However, G. Zhang et al. (2020) suggested that the annual mean DMWS displayed a declining trend of $-0.038 \text{ m s}^{-1} \text{ decade}^{-1}$ over China during 1975–2016. Therefore, the different studies are accompanied by different results. The long-term trends of DMWS also show regional differences. For example, the annual average maximum wind speed over China's Shandong Province presented a decreasing trend of $-0.14 \text{ m s}^{-1} \text{ decade}^{-1}$ (Dong et al. 2018), which was stronger than the national averaged. Although the DMWS values and their trends

show regionality, almost all studies proposed that the large-scale circulation changes, such as those of the North Atlantic (NAO) and the Arctic Oscillation (AO), accounted for the changes in the historical DMWS (Yan et al. 2002; G. Zhang et al. 2020). Global warming induced by the emission of greenhouse gases (GHGs) could be another factor for the regional DMWS changes over land; in particular, the Southern Hemisphere temperature exhibited a significant effect on the distinct oceanic and continental trends in DMWS (Yan et al. 2002). Based on three global climate models (GCMs), Jiang et al. (2013) projected that the annual maximum wind speed will decrease during 2046–65 and 2080–99 relative to 1980–2000; however, the performance of GCMs in simulating the observed annual maximum wind speed is not estimated. Kumar et al. (2015) discovered that the CMIP5 multimodel ensemble captures spatial characteristics of the annual maximum wind speed over the Northern Hemisphere; however, the historical trend in annual maximum wind speed is not represented in most CMIP5 models. The performance of GCMs in simulating the observed DMWS must be estimated before the DMWS is projected, due to this processing method can pick out the good models, and therefore can reduce the uncertainty of the projected results.

Multidecadal changes in the observed maximum or mean wind speeds over China have been analyzed (G. Zhang et al. 2020; Zha et al. 2021b), but the projection of DMWS lacks systematic investigation. Strong winds can damage buildings, infrastructure, and crops, resulting in large economic losses (G. Zhang et al. 2020); meanwhile, strong winds can significantly influence the frequency of dust storms and air quality (Guo et al. 2011), and the wind erosion of soils in some regions of the world (G. Zhang et al. 2019). In the last decade, economic and insured losses due to extreme winds have witnessed unprecedented increases (Kumar et al. 2015). In September 2020, China pledged to peak carbon dioxide emissions before 2030 and achieve carbon neutrality before 2060 (Sherman et al. 2021). Wind energy is clean and reproducible, and the efficient development and use of wind energy can help China accomplish its goals of peaking carbon dioxide emissions and achieving carbon neutrality. Wind speed changes affect wind energy (Karnauskas et al. 2018), whereas wind electricity production is determined by instant winds (e.g., DMWS), as the magnitude of the wind power is proportional to the cube of the instant wind speed (G. Zhang et al. 2020). Furthermore, the Intergovernmental Panel on Climate Change (IPCC) Sixth Assessment Report (AR6) pointed out the estimated results of extreme wind speed changes, and the corresponding trends show low confidence (IPCC 2021). Evidently, we urgently need to carry out the projection of DMWS. A robust assessment and projection of DMWS not only is beneficial to improve our understanding of extreme climate change in the future (Vose et al. 2014), but also is required for the assessment of wind energy and the prediction of environmental and ecological issues related to DMWS (Azorin-Molina et al. 2016).

In this study, the performance of CMIP6 GCMs in simulating the spatiotemporal characteristics in DMWS over China is estimated, and the future changes of DMWS under

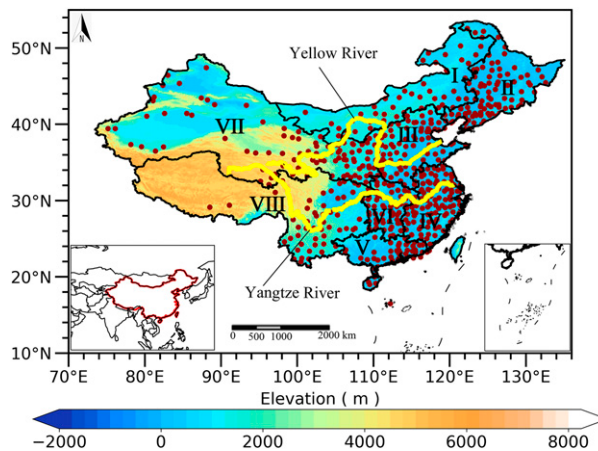


FIG. 1. Distribution of the selected 564 meteorological stations (red dots) and the terrain height (shading) over China. Yellow lines depict the Yellow River and Yangtze River. To estimate the regional difference in daily maximum wind speed in CMIP6, China is divided into eight subregions: I (Inner Mongolia), II (Northeast China), III (North China), IV (East China), V (South China), VI (Central China), VII (Northwest China), and VIII (Southwest China). The location of China in East Asia is shown in the inset.

different shared socioeconomic pathways (SSPs) is projected. Meanwhile, the strength in forcing scenario influencing the variability in DMWS is unraveled, and the differences of future DMWS changes compared with the mean wind speed are discussed. This study provides a reference for improving our understanding of DMWS changes; meanwhile, it also provides a scientific basis for decision-makers to formulate policies to deal with climate change.

2. Datasets and methods

a. Datasets

The domain of this study encompasses all of China (16° – 54° N, 75° – 136° E). The topography of the study area is shown in Fig. 1. The projections of DMWS are based on CMIP6 datasets, which are available at <https://esgf-node.llnl.gov/search/cmip6>, last accessed on 10 September 2021. The monthly mean DMWS outputs from nine CMIP6 GCMs are available at the time of this analysis, and therefore these models are used

(Table 1). The monthly mean DMWS value is calculated based on the daily maximum near-surface wind speed (usually 10 m). CMIP6 datasets include multiple runs from certain GCMs that are selected based on the “ripf” index, which represents the initial state (realization r), the initialization method (i), the physics version (p), and the forcing dataset (f) (Akinsanola et al. 2020; Parding et al. 2020). For each model, the monthly mean values of DMWS with the first realization (r1l1p1f1) for both the historical and the projected scenarios are used (Grose et al. 2020; Jian et al. 2020). The historical and future simulations span the periods of 1850–2014 and 2015–2100, respectively. The physical parameterizations and spatial resolution of CMIP6 have been improved compared to those in CMIP5 (Eyring et al. 2016, 2019). The model’s performance is assessed by comparing the simulations with the observations. The multimodel ensemble (MME) of CMIP6 can reduce the uncertainty (Akinsanola et al. 2020), and therefore it is applicable to project future changes in DMWS, for which SSP126, SSP245, SSP370, and SSP585 are considered (Bai et al. 2020; Cook et al. 2020). The SSPs represent a range of future GHGs and land use change scenarios estimated from integrated assessment models (IAMs) and based on various assumptions regarding economic and population growth, investment in health and education, climate mitigation efforts, and global governance (Adhar and Mishra 2020). Based on the introductions of O’Neill et al. (2016), SSP126 represents the low end of the range of future forcing pathways in the IAM literature and updates the RCP2.6 pathway. SSP126 is anticipated to produce a multimodel mean of significantly less than 2°C warming by 2100, and therefore can support analyses of this policy goal. SSP245 represents the medium part of the range of future forcing pathways and updates the RCP4.5 pathway. SSP370 represents the medium to the high end of the range of future forcing pathways, which fills a gap in CMIP5 forcing pathways that are particularly important because it represents a forcing level that is similar to forcing in the SSP2 baseline scenario as well. SSP585 represents the high end of the range of future pathways in the IAMs. SSP126, SSP245, SSP370, and SSP585 result in an end-of-century radiative forcing of 2.6, 4.5, 7.0, and 8.5 W m^{-2} , respectively (Wang et al. 2019; Cook et al. 2020).

To estimate the performance of CMIP6 in simulating historical DMWS changes, the observed DMWS is employed for making comparison with simulations. DMWS was measured using an anemometer placed 10 m above the ground at each

TABLE 1. Primary parameters of Coupled Model Intercomparison Project Phase 6 (CMIP6) models used in this study.

No.	Model name	Institution	Resolution	Country
1	AWI-CM-1-1-LR	Alfred Wegener Institute	192×288	Germany
2	CMCC-CM2-SR5	Fondazione Centro Euro-Mediterraneo sui Cambiamenti Climatici	192×288	Italy
3	CMCC-ESM2	CMCC Earth System Model	192×288	Italy
4	EC-Earth3	EC-Earth Consortium	256×512	EC
5	GFDL-ESM4	National Oceanic and Atmospheric Administration, Geophysical Fluid Dynamics Laboratory	180×288	United States
6	IPSL-CM6A-LR	Institute for Pierre Simon Laplace	143×144	France
7	MPI-ESM1-2-HAM	Max Planck Institute for Meteorology	96×192	Germany
8	MPI-ESM1-2-HR	Max Planck Institute for Meteorology	192×384	Germany
9	MPI-ESM1-2-LR	Max Planck Institute for Meteorology	96×192	Germany

meteorological station. The site of stations, installation of anemometers, and the observation process were conducted according to the World Meteorological Organization's Guide to Global Observation Systems (CMA 2003). The observed dataset was obtained from the National Meteorological Information Center (NMIC) (<http://data.cma.cn/>; last accessed 1 February 2023), which has been examined and calibrated by the NMIC using the climate threshold test, station extreme test, and temporal and spatial consistency tests. Detailed introductions about these quality-control methods have been shown in the former studies (Wang et al. 2007; Wang 2008; Wan et al. 2010). According to the above tests, the correct data, questionable data, and incorrect data were labeled with the quality control codes 0, 1, and 2, respectively.

b. Methods

To obtain a high-quality wind speed record at each meteorological station and improve the robustness of the results, the selected stations must conform to the following criteria: 1) the station must be a national meteorological station; 2) the DMWS must be accompanied by the quality control code "0" in the datasets; 3) there were no missing data in a whole year after 1980, and no missing data during a whole season and month in each year; and 4) the total days of the missing data accounting for less than 1.0% of the length of the entire data sequence.

After the quality control, the standard normal homogeneity test (SNHT) and Pettitt test are employed to examine the homogeneity of the selected stations. These methods have been used in former studies (Alexandersson 1986; He et al. 2012; Shen et al. 2021a). The SNHT can be presented using Eq. (1):

$$Q_i = \frac{Y_i \sum_{j=1}^n R_j^2}{\sum_{j=1}^n (\rho_j^2 X_{ji} \bar{Y}/\bar{X}_j)}, \quad (1)$$

where Q_i is a reference function, Y_i denotes the DMWS of the tested station in i year, \bar{Y} denotes the mean DMWS in the tested station, X_{ji} denotes the mean DMWS in j reference station in i year, \bar{X}_j is the mean value of DMWS in j reference station, R_j is the correlation coefficient between the reference and tested stations, and n is the total number of reference stations. The reference stations are picked out based on the following criterion: If the stations are enclosed with a circle with radius of 1° latitude and longitude centered at the middle of the tested stations, the stations are selected as the reference stations (Li et al. 2003). As the SNHT method is sensitive to the start and end points of a sequence, a nonparametric Pettitt test is employed to examine the stations that pass the SNHT. For a time sequence $x_1, x_2, x_3, \dots, x_n$, its rank sequence is $r_1, r_2, r_3, \dots, r_n$. The rank sequence can be used to define a statistic S_k , which can be expressed by Eq. (2):

$$S_k = 2 \sum_{i=1}^k r_i - k(n-1), \quad k = 1, 2, 3, \dots, n, \quad (2)$$

where $r_i = +1, 0$, and -1 when $x_i > x_j$, $x_i = x_j$, and $x_i < x_j$, respectively. If the maximum S_k is larger than the threshold of the Pettitt test ($p < 0.05$), the i th year is defined as the mutation point. More details about the homogenization methods can be found in Akinsanola and Ogunjobi (2017) and Shen et al. (2021a). Based on the SNHT and Pettitt test, 564 stations that pass the homogenization test are selected for the analysis in this study (Fig. 1). To evaluate the performance of the CMIP6 GCMs in simulating the monthly DMWS changes, the month-to-month difference in DMWS is analyzed using Eq. (3):

$$\text{MWD} = V_{i+1} - V_i \quad (i = 1, 2, 3, \dots, 11), \quad (3)$$

where MWD denotes the month-to-month difference in DMWS. To assess the effects of the strengthening in forcing scenario on the MWD, the difference between the 90th and 10th percentiles of MWD is calculated using Eq. (4)

$$\text{MWD}_V = |\text{MWD}_{90\text{th}} - \text{MWD}_{10\text{th}}|, \quad (4)$$

where $\text{MWD}_{90\text{th}}$ and $\text{MWD}_{10\text{th}}$ denote the 90th and 10th percentiles of MWD, respectively.

The correlation coefficient and root-mean-square error (RMSE) between the observations and model outputs are employed to evaluate the performance of CMIP6 GCMs in simulating the DMWS (Song and Zhou 2014; Peng et al. 2020). To lay a baseline for assessing future changes, the historical runs for the period 1995–2014 are used to determine the present-day climate (Wang et al. 2020). To estimate the performance of CMIP6 in simulating the observed DMWS, based on the bilinear interpolation technique (Z. Chen et al. 2020), the wind speed in CMIP6 is interpolated to the stations, and compared with the observed historical DMWS. Different models with different spatial resolution, for future projections, in order to compute the multimodel ensembles, all CMIP6 datasets are gridded to a common grid of $1.0^\circ \times 1.0^\circ$ (latitude \times longitude) using a bilinear interpolation technique. The bilinear interpolation technique has been judged to be the least suitable for the transfer of the grid forecast field to another or discrete observation field (Wu et al. 2016, 2017, 2018b). More details about this method can be found in Accadia et al. (2003) and Mastylo (2013). The DMWS trend is calculated based on the least squares method, and the two-tailed Student's t test is used to examine the significance of the trend and correlation coefficient. For future projections, we focus on three specific periods: the near-term (2021–40), midterm (2041–60), and long-term (2081–2100) (Jiang et al. 2020). Four seasons are defined as boreal winter (December, January, and February), spring (March, April, and May), summer (June, July, and August), and autumn (September, October, and November). To estimate the performance of CMIP6 GCMs in simulating the regional DMWS changes, China is divided into eight subregions: Inner Mongolia (44 stations), Northeast China (87 stations), North China (77 stations), East China (98 stations), South China (42 stations), Central China (62 stations), Northwest China (99 stations), and Southwest China (55 stations) (Fig. 1).

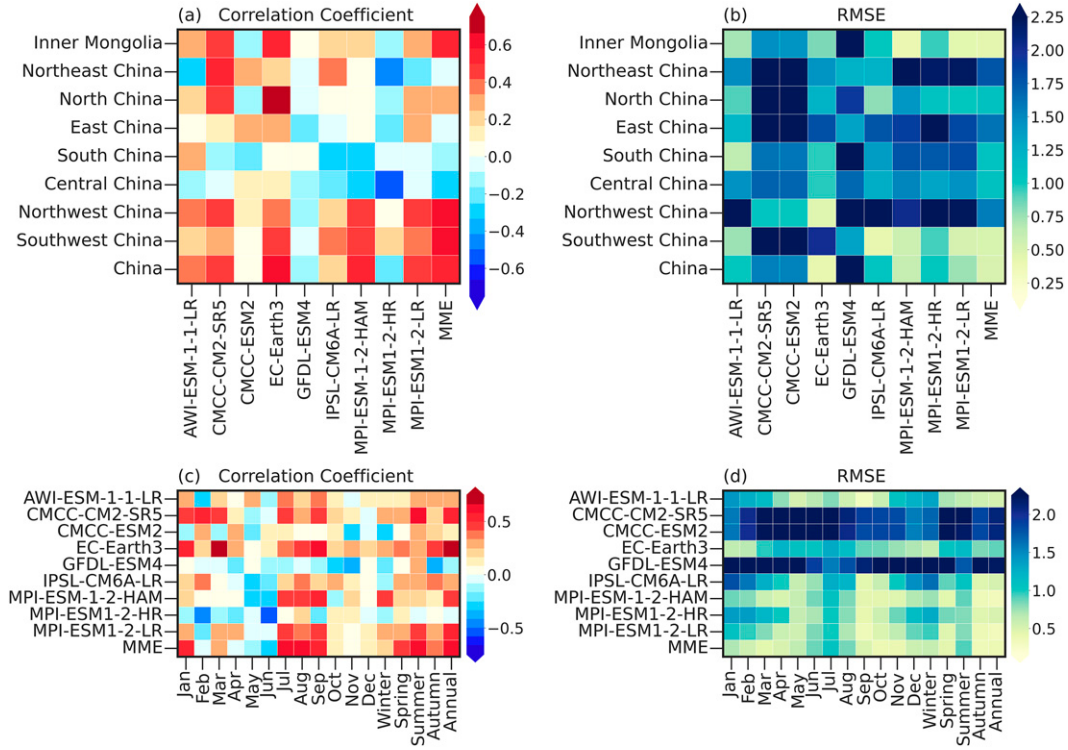


FIG. 2. Heat maps of the (a) correlation coefficient and (b) root-mean-square error (RMSE; unit: m s^{-1}) between observations and CMIP6 models over different regions in China from 1980 to 2014. (c),(d) As in (a) and (b), respectively, but for different seasons and months. In (a) and (b), the horizontal axis denotes the model's name, and the vertical axis is the area division. In (c) and (d), the horizontal axis denotes the time scales, and the vertical axis lists the model's name. The correlation coefficient and RMSE are calculated based on the annual mean DMWS.

3. Results

a. DMWS climatology comparison between observations and CMIP6

To assess the uncertainty of the projected results, the relationships between observations and CMIP6 over all of China and its eight subareas are analyzed (Fig. 2). CMIP6 and observations showed a positive correlation across all of China, except for GFDL-ESM4 and MPI-ESM1-2-HR. The largest correlation was found in EC-Earth3 (0.58; $p < 0.01$). A positive correlation was also detected in MME of CMIP6 (0.53; $p < 0.01$). Most CMIP6 models show better performance in simulating the DMWS over northwest China, southwest China, and Inner Mongolia than those over other subregions. CMIP6 models and observations show a negative correlation over south and central China, suggesting most CMIP6 models exhibit poor performance in simulating the observed DMWS over these regions (Fig. 2a). DMWS's RMSE over all of China was smaller than 2.0 m s^{-1} for all CMIP6 models, except for GFDL-ESM4 (RMSE $> 2.7 \text{ m s}^{-1}$). RMSEs showed regional differences among different models. Most CMIP6 models displayed larger RMSEs in simulating the DMWS over northeast and northwest China. Across all of China and most subareas, the smallest RMSE was found in the MME of CMIP6. The RMSE in MME of CMIP6 was smaller than 0.50 m s^{-1} for the

regional average of entire China (Fig. 2b). The correlation coefficient and RMSE between the observations and CMIP6 at different time scales are also analyzed. Most CMIP6 models and observations also showed positive correlations at different time scales. The MME of CMIP6 had a larger correlation coefficient than the single model, and the largest correlation was found in the annual mean (0.62; $p < 0.01$). Larger correlation coefficients were also found for seasonal results in the MME of CMIP6 than those in the single model (Fig. 2c). The RMSE exhibited large discrepancies in different models at different time scales, which were larger from CMCC-CM2-SR5, CMCC-ESM2, and GFDL-ESM4 than other models. Compared to a single model, a smaller RMSE was found in the MME of CMIP6 ($< 0.75 \text{ m s}^{-1}$) (Fig. 2d). Briefly, the CMIP6 models exhibit regional differences in simulating the DMWS over China. Moreover, the DMWS changes in the MME of CMIP6 were more effective than those in a single model at different time scales. Consequently, the MME of CMIP6 is considered in the following sections.

Spatial patterns of mean DMWs in the observations and MME of CMIP6, as well as the DMWS difference between the observations and MME of CMIP6 during all four seasons, are analyzed (Fig. 3). The large values of observed DMWS located mainly in Inner Mongolia, northeastern China, and western China, reaching up to 6.0 m s^{-1} in most

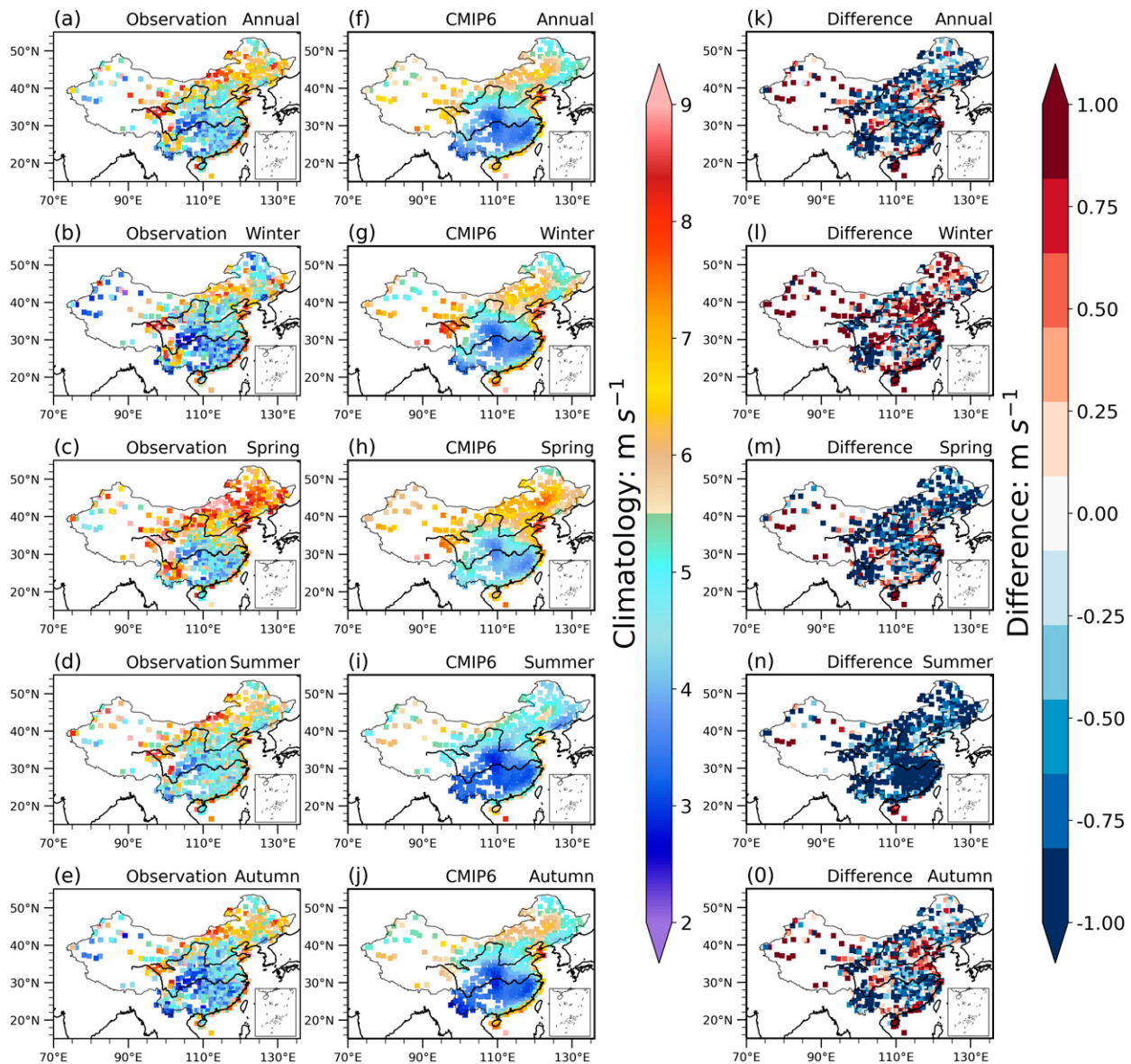


FIG. 3. Spatial patterns of annual and seasonal means of DMWS in the (a)–(e) observations and (f)–(j) multimodel ensemble of CMIP6 (unit: m s^{-1}), as well as (k)–(o) the annual and seasonal DMWS biases between the MME of CMIP6 and observations from 1980 to 2014 (unit: m s^{-1}), showing the (a),(f),(k) annual mean, (b),(g),(l) winter, (c),(h),(m) spring, (d),(i),(n) summer, and (e),(j),(o) autumn.

regions. The small values of observed DMWS located mainly in central China and eastern China, falling below 5.0 m s^{-1} in most of these regions (Figs. 3a–e). Seasonally, the observed largest DMWS occurred in spring (5.5 m s^{-1}) (Fig. 3c), and the smallest ones occurred in summer (4.3 m s^{-1}) (Fig. 3d). The spatial patterns of DMWS in CMIP6 were similar to those in the observations, suggesting the MME of CMIP6 efficiently captures the spatial patterns of DMWS climatology (Figs. 3f–j). Similar to the observations, the CMIP6 simulated DMWS also showed seasonal differences. The DMWS differences between the observations and simulations did not present consistent positive or negative biases; however, the DMWS climate state was underestimated

in all seasons by CMIP6, except for winter (0.01 m s^{-1}) (Fig. 3l). The largest DMWS biases occurred in summer (-0.74 m s^{-1}), and the smallest ones appeared in winter (0.01 m s^{-1}).

The observed annual and seasonal mean DMWS showed decreasing trends over China (Figs. 4a–e). For the spatial average, the strongest decrease in DMWS was found in spring ($-0.41 \text{ m s}^{-1} \text{ decade}^{-1}$, $p < 0.01$), and the weakest decrease in DMWS was found in autumn ($-0.33 \text{ m s}^{-1} \text{ decade}^{-1}$, $p < 0.01$). Compared with the observations, a decreasing trend was also detected for the annual and seasonal mean DMWS in MME of CMIP6 (Figs. 4f–j). The largest and smallest spatial correlation coefficients were found in autumn and

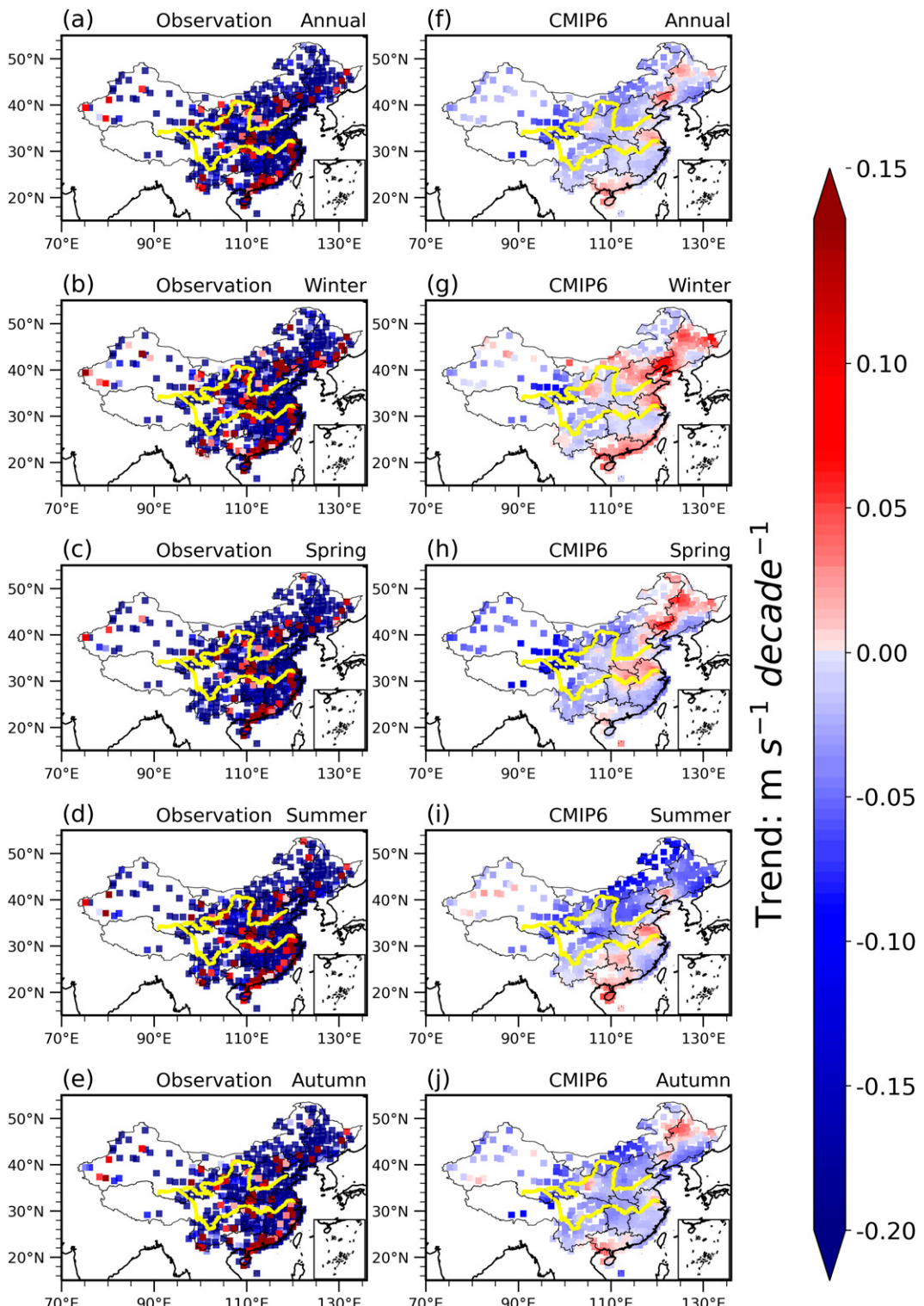


FIG. 4. Spatial patterns of DMWS trends in (a)–(e) the observations and (f)–(j) the MME of CMIP6 from 1980 to 2014 (unit: $\text{m s}^{-1} \text{decade}^{-1}$): (a),(f) annual mean, (b),(g) winter, (c),(h) spring, (d),(i) summer, and (e),(j) autumn.

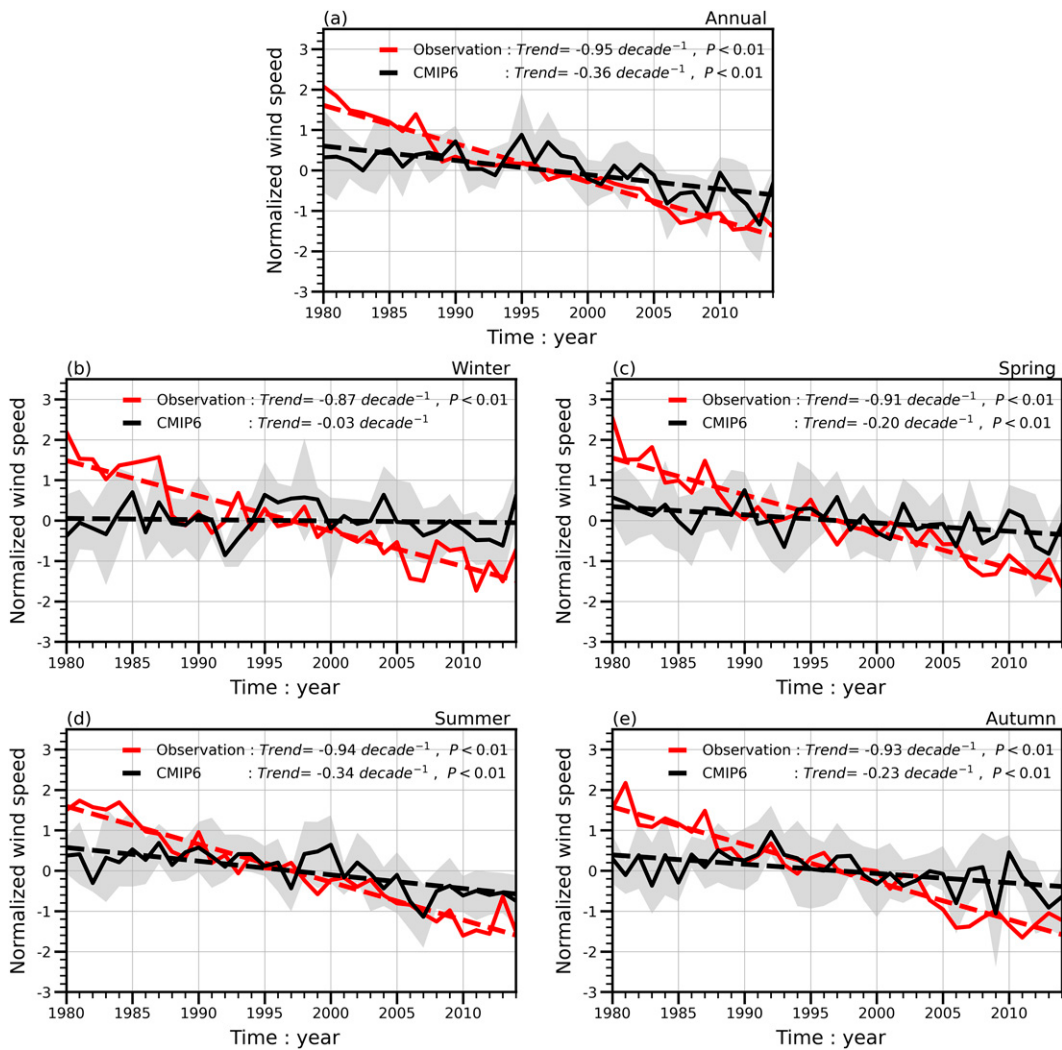


FIG. 5. Temporal evolutions of DMWS from 1980 to 2014, for the (a) annual mean, (b) winter, (c) spring, (d) summer, and (e) autumn. Red and black lines represent observations and MME of CMIP6, respectively. The shading denotes the uncertainty spread determined by all CMIP6 models. The dashed lines denote linear fit curves. Trends during the study period are presented using the inset text. In the text, $p < 0.01$ denotes that the trend passes the significance t test at the 0.01 level.

annual mean, with values of 0.69 and 0.41, respectively; meanwhile, these spatial correlation coefficients passed the significant t test at the 0.01 level. However, the trends of DMWS in CMIP6 were smaller in magnitude than those in the observations, and which also showed seasonal and regional differences. Quantitatively, 79.1%, 49.9%, 66.7%, 73.4%, and 82.6% of total stations exhibited DMWS reduction in MME of CMIP6 for annual mean, winter, spring, summer, and autumn, respectively. For annual mean DMWS in the MME of CMIP6, a strong decrease was found in Inner Mongolia and northwest China (Fig. 4f). For the seasonal mean DMWS in the MME of CMIP6, a weak increase was detected over northeast China and south China (Fig. 4g). A strong decrease in the DMWS was found in summer (Fig. 4i), especially over northeast China, Inner Mongolia, north China,

and northwest China, in which the decreasing trends reached $-0.12 \text{ m s}^{-1} \text{ decade}^{-1}$ ($p < 0.01$).

b. Temporal changes in DMWS between observation and CMIP6

Annually, both the observations and MME of CMIP6 exhibit that the DMWS decreased from 1980 to 2014, at rates of -0.95 ($p < 0.01$) and $-0.36 \text{ decade}^{-1}$ ($p < 0.01$), respectively. The decreasing trend of DMWS in MME of CMIP6 was smaller than those in the observations, which accounted for approximately 38.0% of the observed decreasing trend. The correlation coefficient of DMWS between observations and MME of CMIP6 was 0.67 ($p < 0.01$) (Fig. 5a). The decreasing trend in DMWS was also detected for both the observations and MME of CMIP6 during all four seasons. The weakest reduction was found in winter,

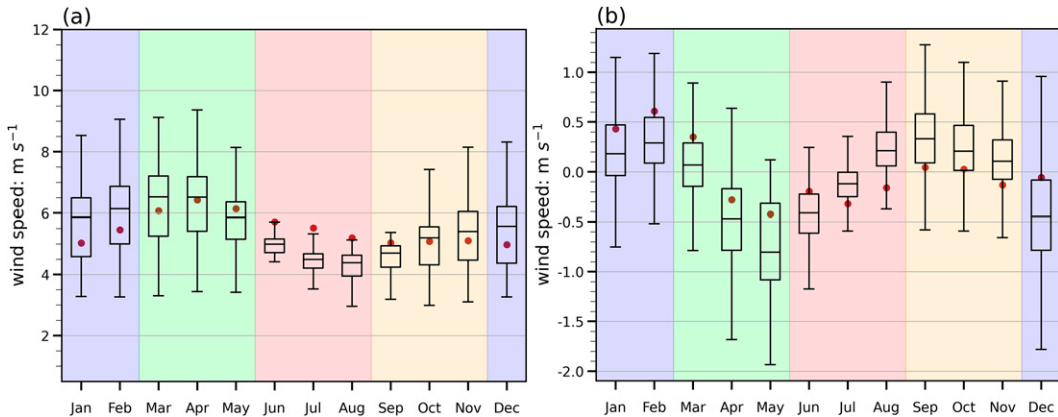


FIG. 6. (a) Box-and-whisker plots of monthly mean DMWS in MME of CMIP6 over China from 1980 to 2014 (units: m s^{-1}), and (b) month-to-month DMWS difference in observation (red dots) and MME of CMIP6 (box-and-whisker plots). In (a) and (b), red dots represent the observed monthly mean DMWS. The mean value (middle lines), 25th and 75th percentile range (boxes), and 10th and 90th percentile range (upper and lower horizontal lines) are presented in a box-and-whisker plot. The months with light blue, light green, pink, and light yellow denote winter, spring, summer, and autumn, respectively.

at the rates of -0.87 ($p < 0.01$) and -0.03 decade $^{-1}$ ($p > 0.10$) in observations and MME of CMIP6, respectively (Fig. 5b), and the strongest reduction was found in summer, at rates of -0.94 ($p < 0.01$) and -0.34 decade $^{-1}$ ($p < 0.01$) in observations and MME of CMIP6, respectively (Fig. 5d). Correlation coefficients of temporal sequences between the observations and MME of CMIP6 were 0.20 , 0.50 , 0.67 , and 0.43 for the winter, spring, summer, and autumn, respectively, which passed the significance t test at a 0.10 level. Consequently, the MME of CMIP6 is able to reproduce the decreasing trend of the observed DMWS, although the magnitude of trend was smaller than those in the observations. In comparison to the performance of CMIP5 in simulating the trend of mean wind speed (Chen et al. 2012; Jiang et al. 2018; Wu et al. 2020), the trend of DMWS simulated by CMIP6 was closer to those in the observations. The fully coupled GCMs are not temporally synchronous with the real world in historical monthly to interannual variability (Karnauskas et al. 2018), so the interannual variability in DMWS in CMIP6 is not consistent with those of the observations. In this study, we mainly focused on the climatology and long-term trends of DMWS and estimated whether the CMIP6 can simulate the long-term reduction in DMWS. Therefore, the discrepancies in DMWS changes from historical monthly to interannual do not affect our focus. As is well known, unlike the temperature and precipitation, GCMs simulating the DMWS show great uncertainty (IPCC 2021), even though several GCMs simulate an increasing trend in DMWS (Chen et al. 2012; Wu et al. 2020). If the MME of CMIP6 cannot simulate the decreasing trend in DMWS, the MME of CMIP6 could not be used to project the climatology and long-term changes in DMWS.

The ability of CMIP6 to simulate the seasonal cycle is likewise a crucial index used in the estimation of CMIP6 performance (Fig. 6). The observed DMWS exhibited seasonal changes, with the strongest DMWS value occurring in spring (a maximum of 6.52 m s^{-1} in April) and the weakest DMWS value occurring in summer (a minimum of 4.38 m s^{-1} in

August). Additionally, the observed DMWS increased from January to April and decreased from April to August. Similar characteristics were likewise captured by CMIP6 (Fig. 6a). Generally, the interquartile model spreads (boxes) of DMWS were larger in winter and spring and smaller in summer. These results indicate that the large interannual changes in DMWS appeared during winter and spring, and relatively small interannual changes in DMWS appeared during summer. In comparison to previous studies, the monthly changes in DMWS were consistent with those of the mean wind speed (Guo et al. 2011). The month-to-month wind speed difference (denoted by MWD) in the observations and CMIP6 was also explored (Fig. 6b), which showed marked seasonal changes. The largest positive and negative MWD appeared in February (0.28 m s^{-1}) and May (-0.80 m s^{-1}), respectively. Furthermore, the observed MWD decreased from January to May, and from September to December, whereas it increased from May to September. Similar results were reproduced by the CMIP6. In summary, CMIP6 reproduced not only the observed monthly DMWS changes, but also the observed MWD changes.

c. Projected changes in DMWS over China based on CMIP6

Future DMWS change shows decreasing trend under four SSPs, and the decreasing trend is enhanced accompanied by the strengthening of the SSP. The reduction in future DMWS under all SSPs is also reproduced in the intermodel spreads of all the models. Notably, DMWS with SSP126 shows a significant decrease before 2041, whereas the reduction does not appear after 2041. In brief, the lower-emission scenario could avoid the long-term weakening of the DMWS in China (Fig. 7a). Additionally, the DMWS exhibits different trends among varied periods, although they mainly show a long-term slowing in the future. DMWS exhibits reduction during all

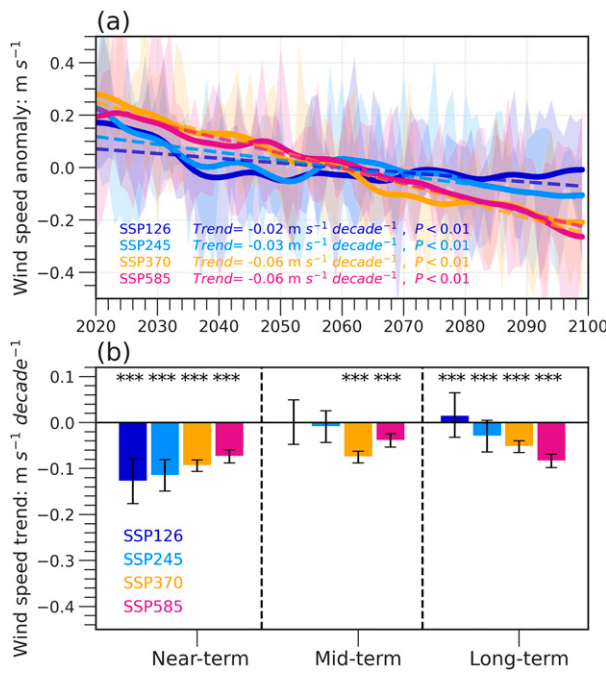


FIG. 7. (a) Temporal changes of annual mean DMWS anomalies (9-yr Gaussian low-pass filter) over China and (b) projected DMWS trends for the near-term (2021–40), midterm (2041–60), and long-term (2081–2100) under different SSPs. In (a) and (b), SSP126 (dark blue), SSP245 (light blue), SSP370 (yellow), and SSP585 (red). In (a), the dashed lines denote the linear fit curves, the shadings denote the intermodel spreads of all CMIP6 models, and $p < 0.01$ denotes that the trend passes the significance t test at the 0.01 level. In (b), the black bar denotes the uncertainty of the result calculated based on all CMIP6 models. Three asterisks (****) indicate that the trend passes the significance t test at the 0.01 level.

periods, except for the long term (2081–2100) with SSP126. For the near-term period (2021–40), the decreasing trend weakened accompanied by the strength in forcing scenario, at rates of -0.13 ($p < 0.01$), -0.11 ($p < 0.01$), -0.09 ($p < 0.01$), and $-0.08 \text{ m s}^{-1} \text{ decade}^{-1}$ ($p < 0.01$) in SSP126, SSP245, SSP370, and SSP585, respectively. In contrast, for the mid- and long-term periods, the decreasing trend is enhanced accompanied by the strengthening in the forcing scenario, especially for the long term. As for the near-, mid-, and long-term periods, the DMWS only shows an increase in the long-term period under SSP126 ($0.02 \text{ m s}^{-1} \text{ decade}^{-1}$; $p < 0.10$); however, the uncertainty (error bar) of the increasing trend is considerable. Consequently, the projected trend in DMWS under SSP126 for the long term could show low confidence, and therefore more care is needed in inferring this result.

Spatial patterns of DMWS trends relative to the current climate during different periods are analyzed under all four SSPs (Fig. 8). The DMWS trends exhibit spatial differences during different periods with different SSPs. For the near term (2021–40) (Figs. 8a–d), DMWS displays a decreasing trend over China, and the most significant reduction is found in western China, reaching up to $-0.03 \text{ m s}^{-1} \text{ decade}^{-1}$ ($p < 0.01$). The

DMWS also exhibits a weak increase over southeastern China for the near term with all SSPs, except for SSP370. The spatial characteristics of DMWS trends during the midterm and long term are not consistent with that of the near term. For the midterm period (Figs. 8e–h), the DMWS with SSP126 shows an increasing trend over the northern parts of the Yellow River and a decreasing trend over southwestern and southeastern China (Fig. 8e). Nevertheless, under SSP245, the decreasing trends in DMWS are found mainly in southwestern and northeastern China (Fig. 8f). For high-emission scenarios (e.g., SSP370 and SSP585), the DMWS mainly shows decreasing trends across China during the midterm period, and the decreasing trends are more significant over northeastern China and the low reaches of the Yellow and Yangtze Rivers under SSP370, and the Tibetan Plateau under SSP585 ($>-0.03 \text{ m s}^{-1} \text{ decade}^{-1}$). Concerning the long term (Figs. 8i–l), the DMWS under SSP126 mainly exhibits an increasing trend in China; in particular, the increasing trend is significant over southern parts of the Yangtze River with SSP126 (Fig. 8i) and the Tibetan Plateau with SSP245 (Fig. 8j). Accompanied by the high-emission scenarios (e.g., SSP370 and SSP585) (Figs. 8k–l), the decreasing trend in DMWS is significant across the Tibetan Plateau. These results testify to the DMWS trends exhibit regional differences with different SSPs and periods.

Figure 9 illustrates the spatial patterns of DMWS changes relative to the current climate under four SSPs. Concerning the near term (Figs. 9a–d), as the forcing scenario strengthens from SSP126 to SSP585, the DMWS experiences a small reduction across entire China, except for some regions of southeastern China. For the midterm (Figs. 9e–h), the spatial patterns of wind speed differences under four SSPs are similar to those of the near term; however, the DMWS difference in the midterm is stronger. For the long term (Figs. 9i–l), the DMWS differences are also larger than those of the near term and midterm. It is worth noting that the DMWS difference presents a similar spatial distribution during different periods with the same forcing scenario, implying that the changes in SSP do not significantly alter the mean climate state of DMWS. Compared to the DMWS trends (Fig. 8), the effects of strength in the forcing scenario on the spatial changes in DMWS differences are relatively small, suggesting the strength in the forcing scenario has a stronger effect on the DMWS trend than DMWS mean value. Furthermore, the future DMWS changes relative to the current climate mainly show positive values ($>0.2 \text{ m s}^{-1}$; $p < 0.10$) over southeastern China.

Seasonal characteristics of DMWS differences (future minus present-day) and trends under four SSPs were further compared (Fig. 10). The DMWS differences show seasonal features (Figs. 10a–c). Negative DMWS differences are found in four seasons, which are below -0.5 m s^{-1} for all three periods. The stronger SSP corresponds to the larger DMWS differences. These results imply that future DMWS might decrease relative to the current climate during four seasons; however, the effects of the strength of forcing scenario on DMWS are not linear. Namely, the DMWS difference relative to the current climate does not strictly increase (decrease) with the strengthening (weakening) of SSPs. Apart from the seasonal differences in DMWS changes relative to the current climate, the

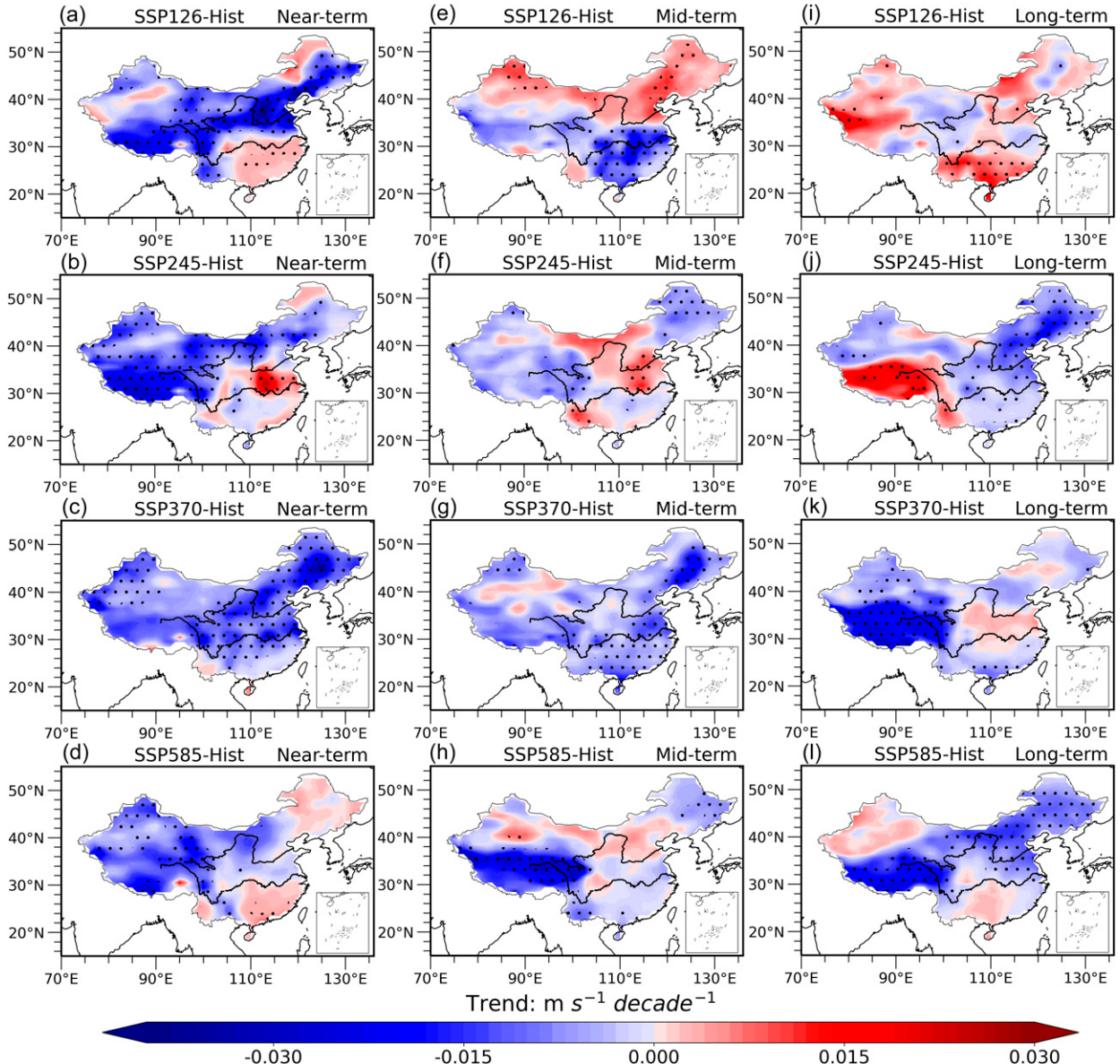


FIG. 8. Spatial patterns of DMWS trends relative to the current climate during (a)–(d) near-term (2021–40), (e)–(h) midterm (2041–60), and (i)–(l) long-term (2081–2100) under (a),(e),(i) SSP126, (b),(f),(j) SSP245, (c),(g),(k) SSP370, and (d),(h),(l) SSP585 (unit: $\text{m s}^{-1} \text{decade}^{-1}$). The region with black dots denotes the trend passes the significance t test at the 0.10 level.

DMWS trends also differ among different seasons (Figs. 10d–f). The DMWS decreases during the near term, and the decreasing trends are more significant with strong scenarios than those with weak ones (Fig. 10d). Seasonal differences in DMWS trends during the mid- and long terms are more evident than those during the near term. The DMWS differences show a smaller uncertainty than the DMWS trends. The uncertainty of the projected DMWS trends for the midterm and long term could also be higher than those for the near term.

We also estimate the seasonal cycle of DMWS (Fig. S1 in the online supplemental material) and the month-to-month wind speed difference (MWD) (Fig. S2) under four SSPs.

Results show that the monthly changes in future DMWS are consistent with the historical DMWS. The largest DMWS appeared in April, with the values of 6.90, 6.94, 6.87, and 6.95 m s^{-1} under SSP126, SSP245, SSP370, and SSP585, respectively. The smallest DMWS is found in August, with values of 4.29, 4.30, 4.15, and 4.29 m s^{-1} under SSP126, SSP245, SSP370, and SSP585, respectively. Under four SSPs, the projected DMWS shows an increase from January to April while a decrease from April to August, and subsequently an increase from August to December (Fig. S1). The mean MWD does not show a significant seasonal cycle (middle lines in Fig. S2). In contrast, the seasonal cycle of historical mean

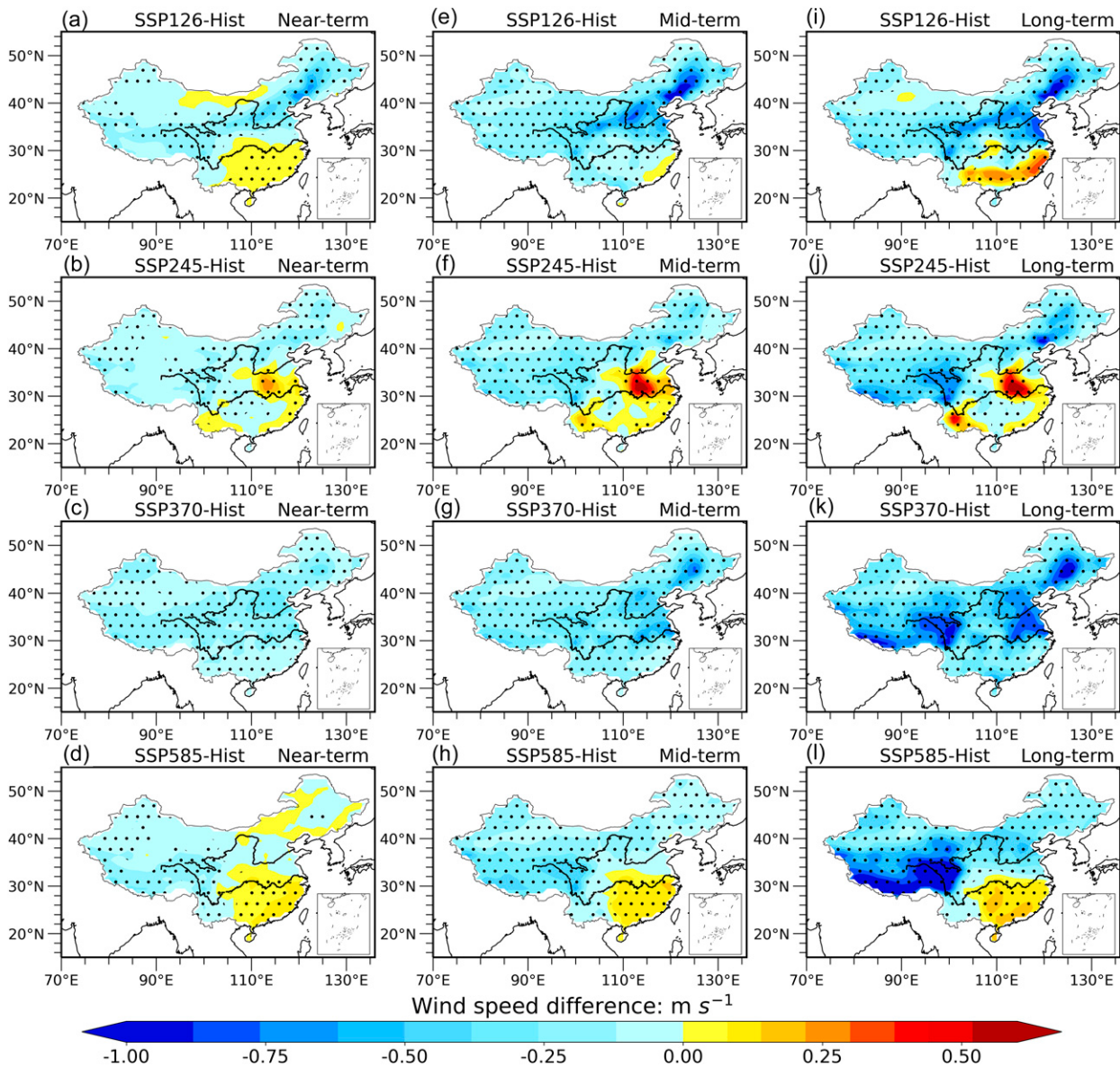


FIG. 9. Spatial patterns of changes in DMWS relative to the current climate over China during (a)–(d) near-term (2021–40), (e)–(h) midterm (2041–60), and (i)–(l) long-term (2081–2100) under (a),(e),(i) SSP126, (b),(f),(j) SSP245, (c),(g),(k) SSP370, and (d),(h),(l) SSP585 (unit: m s^{-1}). The region with black dots denotes the wind speed difference passes the significance *t* test at the 0.10 level.

MWD is evident. Therefore, the MWD of future DMWS (Fig. S2) is not consistent with those of historical DMWS (Fig. 6b). The variations in MWD_s under four SSPs are stronger in winter and spring than those in summer. The MWD_V decreases from January to August, while increases from August to December with four SSPs; however, the stronger forcing scenario leads to a larger MWD_V (Fig. 11). For the seasonal cycle, the mean values of MWD_V with SSP126, SSP245, SSP370, and SSP585 are 1.75, 1.82, 1.87, and 1.96 m s^{-1} , respectively. Hence, it is very likely that the strength in the forcing scenario induces the enhancement of MWD variability.

4. Discussion

Compared with a previous study (G. Zhang et al. 2020), the decreasing trend in future DMWS could be stronger than those in the historical period. The observed annual mean DMWS displayed a significant declining trend of $-0.038 \text{ m s}^{-1} \text{ decade}^{-1}$ for all of China; however, the weakest weakening trend in future DMWS reached $-0.02 \text{ m s}^{-1} \text{ decade}^{-1}$ with SSP126, and the strongest reduction can even reach $-0.06 \text{ m s}^{-1} \text{ decade}^{-1}$. The historical changes in DMWS show regional and seasonal differences (Brönnimann et al. 2012; Wu et al. 2012; Azorin-Molina et al. 2016), and these characteristics also exist in the future DMWS. For future projections, Jiang et al. (2013) have noted

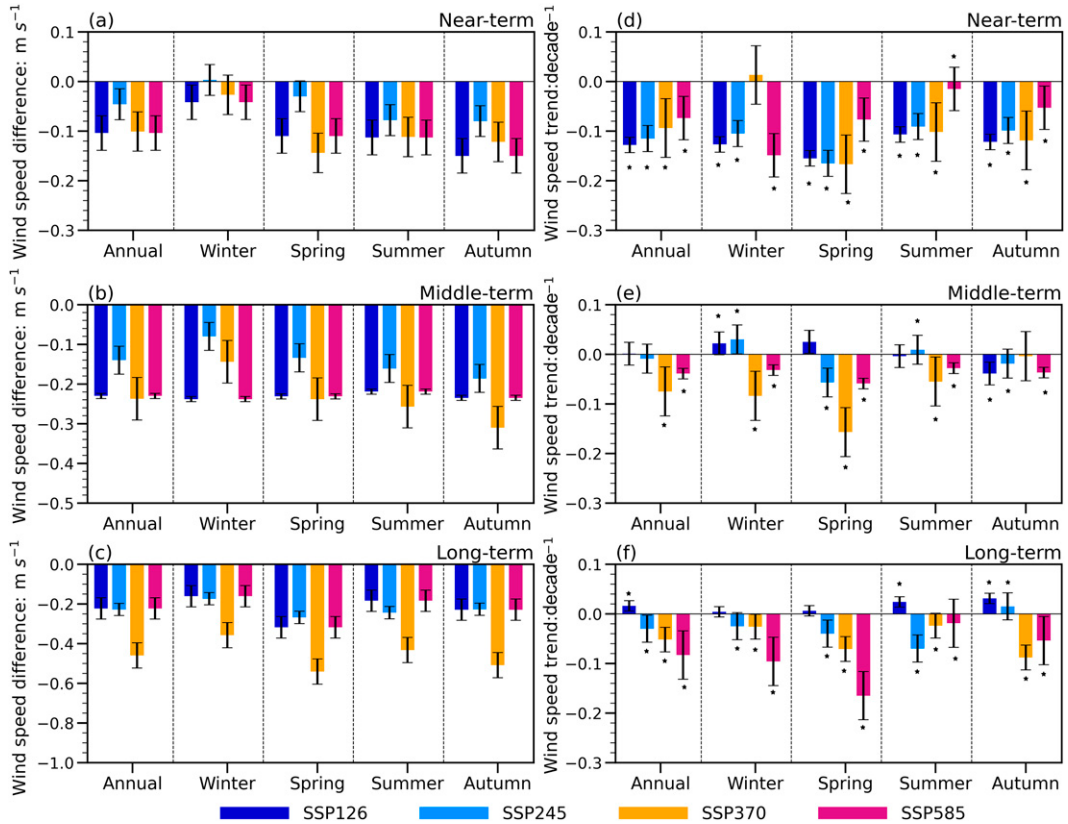


FIG. 10. (a)–(c) DMWS differences (unit: m s^{-1}) and (d)–(f) DMWS trends (unit: decade^{-1}) relative to the current climate during different periods with four SSPs. Black bars denote the uncertainty of the results, which are calculated based on all CMIP6 models. An asterisk (*) denotes that the trend passes the significance t test at the 0.10 level.

that the maximum wind speed across China could decline in the midterm and long term; however, they do not notice the regional differences in wind speed changes; meanwhile, the effects of GHGs on the variability in month-to-month wind speed differences are not unraveled. At the global scale, the annual mean maximum wind speed in the future has been reported to decrease (Kumar et al. 2015). However, at the regional scale, this study

finds that the future DMWS across China also show a long-term reduction. Hence, the slowdown in DMWS could occur under global warming. However, the changes in DMWS at a regional scale are distinct from those at a global scale. The projected annual mean maximum wind speed at a global scale is not likely to increase or decrease significantly as the changes in magnitude and trends of wind speed (Kumar et al. 2015); however, the DMWS in China is projected to reduce significantly. These results mean that the driving mechanism of extreme winds at the global and regional scales could be inconsistent. The changes in extreme winds over land are significantly distinct from those over the ocean. The latter is mainly influenced by tropical cyclones (Yan et al. 2020); however, the former is impacted by more complex factors (Klink 1999). Changes in extreme wind encompass the effects of global warming (Azorin-Molina et al. 2021), and could induce the variations in large-scale ocean-atmosphere circulations (LOACs), such as the southern annual mode and the Indian Ocean dipole (Azorin-Molina et al. 2021), the Atlantic oscillation (Yan et al. 2002), the North Atlantic Oscillation (Azorin-Molina et al. 2016), and the East Asian summer and winter monsoons (Jiang et al. 2013). These LOACs mainly induce the driving forcing changes, namely the pressure-gradient force. Physical mechanisms of the above-mentioned factors affecting extreme wind changes need to be further investigated.

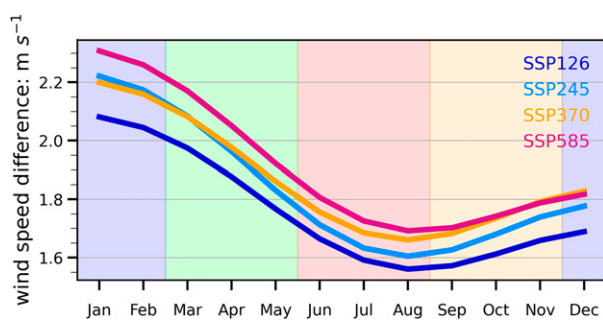


FIG. 11. Changes in the difference between the 90th percentile of MWD and the 10th percentile of MWD. The MWD is the month-to-month DMWS difference. The months with light blue, light green, pink, and light yellow denote winter, spring, summer, and autumn, respectively.

Furthermore, the inherent variability and initial conditions could also exert a strong effect on the projected extreme wind climate throughout the twenty-first century (Pryor et al. 2012).

Compared to the projected changes in the mean wind speed (hereinafter denoted as W_{mean}) (Chen et al. 2012; Wu et al. 2020; Zha et al. 2020, 2021a), the future changes in DMWS (hereinafter denoted as W_{max}) show several different characteristics: 1) The CMIP3/5 mainly exhibits substantial positive bias in the W_{mean} relative to the observations; meanwhile, the spatial fields of the projected W_{mean} are highly similar to those of the historical W_{mean} with comparatively little response to the forcing scenario (Chen et al. 2012). Our study suggests that the CMIP6 GCMs mainly exhibit negative bias in the W_{max} compared to the observations, especially in the summer. Simultaneously, the projected W_{max} relative to the current climate show considerable regional differences from different forcing scenarios. 2) The W_{mean} trend over China is projected to decrease significantly in winter under SSP126, SSP245, and SSP585, and to increase markedly in the summer under SSP585 (Wu et al. 2020). In this study, we uncover that W_{max} in the near term with four forcing scenarios shows a significant decline during all four seasons; however, W_{max} exhibits a significant seasonal difference in the mid- and long-term periods with the changes in SSPs. 3) W_{mean} shows a weak increase in the near term with a low-emission scenario over China (Zha et al. 2021a); however, W_{max} does not show an increase with low-emission scenario in the near term. In contrast, W_{max} increases during the long-term period with high-emission scenario. In brief, the future changes in W_{max} are not consistent with W_{mean} . These results indicate that the physical mechanisms of W_{max} changes could be not consistent with W_{mean} .

The reduction in DMWS can be reproduced in most CMIP6 GCMs, but the ones simulated by CMIP6 are weaker than those in the observations. Indeed, both the CMIP6 GCMs and reanalysis products tend to underestimate the reductions in the observed wind speeds (Torralba et al. 2017). The possible causes include the coarse model resolution (Zha et al. 2021a), failure in reproducing large-scale ocean-atmosphere circulations (Zeng et al. 2019), and some anthropogenic forcing signals, such as GHGs and urbanization (Zha et al. 2017b, 2019; Wu et al. 2018a; Z. Zhang et al. 2019; Shen et al. 2021b; Zhang and Wang 2021). Moreover, the nonclimate factor, such as the suboptimal anemometer calibration, data processing protocols, poor site selection, and site maintenance could also contribute to the reduction in the wind speed (Azorin-Molina et al. 2018; Zha et al. 2021b).

The CMIP6 models cannot truly simulate the observed decreasing trend in DMWS, and some anthropogenic forcing signals cannot be accurately obtained in advance; therefore, for future projections, changes in DMWS could show uncertainty. In this study, we only consider the effects of the forcing scenario on the spatiotemporal changes in future DMWS, whereas how the internal variability and external forcing influence the DMWS need to be further unraveled. Furthermore, investigating on DMWS changes should serve for the wind energy estimation and development, are crucial for wind power generation. The seasonality and interannual changes in

wind speed, and which is influenced mainly by internal variability. However, projections of the internal variability based on the GCMs exhibit high uncertainty (Monerie et al. 2017; Zhou et al. 2020; Zhu et al. 2020; Zha et al. 2021c). Several researchers propose that the large ensembles can be used to extract the effects of external forcing and internal variability (Deser et al. 2012, 2020; Yu et al. 2020), and the comparison of results based on different large ensembles can reduce the uncertainties of internal variability and external forcing effects (Zha et al. 2021c). In addition, the statistical and dynamical downscaling methods can extract the regional and local signals of climate change, and therefore can be used to diminish the error in climate prediction versus observation that was induced by the local characteristics missing in the GCMs (He et al. 2013). Therefore, in the future, bias correction at regional scales carried out by employing the statistical or dynamical downscaling methods could reduce the uncertainties of the projected DMWS (Miao et al. 2016; Costoya et al. 2020).

5. Conclusions

In this study, based on the observed DMWS and CMIP6 datasets, the performance of CMIP6 GCMs is estimated in terms of simulating the spatiotemporal characteristics of DMWS over China. Future changes in DMWS over China are projected, and the differences of changes in mean wind speed and DMWS are discussed. Major results are summarized as follows.

During the historical period from 1980 to 2014, the largest values of observed DMWS are located mainly in Inner Mongolia, northeastern China, and western China, while the smallest ones are located mainly in central and eastern China. The largest and smallest DMWS appear in spring and summer, respectively. The observed DMWS exhibits a significant decrease during four seasons, with the largest reduction in spring ($-0.41 \text{ m s}^{-1} \text{ decade}^{-1}$; $p < 0.01$) and the weakest reduction in autumn ($-0.33 \text{ m s}^{-1} \text{ decade}^{-1}$; $p < 0.01$). CMIP6 models efficiently capture the spatiotemporal characteristics of the observed DMWS, but underestimate its decreasing trends. The DMWS simulated by the CMIP6 show regional and seasonal differences over China. Most CMIP6 models show better performances over northwestern China, southwestern China, and Inner Mongolia than in other regions. Meanwhile, in comparison to the single models, the MME of CMIP6 exhibits a better performance in simulating the spatiotemporal characteristics of DMWS over China.

Future DMWS shows a long-term reduction under all SSPs, and the decreasing trend of DMWS is enhanced accompanied by the strength of the forcing scenario. The DMWS with SSP126 shows a significant decrease before 2040, whereas the significant decrease in DMWS with SSP126 does not appear after 2040, suggesting the lower-emission scenario effectively avoids long-term weakening of the DMWS in the future. Furthermore, the DMWS trend shows regional differences under different SSPs and periods, although their reductive trend is consistent. Relative to the current climate, the DMWS mainly experiences a weak reduction over entire China, except for some regions of southeastern China. The strength in forcing

scenario has a larger effect on the DMWS trend than the DMWS climatology. Compared to the DMWS trends, the effects of strength in the forcing scenario on the spatial changes in DMWS difference are relatively small. Monthly changes in future DMWS under different SSPs are consistent with historical DMWS; however, the month-to-month DMWS difference does not yield a significant seasonal cycle compared to historical DMWS. The strength in the forcing scenario also enhances the variability of the month-to-month DMWS difference.

Acknowledgments. The work is supported by the National Natural Science Foundation of China (42141017, 42005023, 41875178, 41775087), Key Research and Development Program of China (2018YFA0606004), and Swedish Formas (2019-00509 and 2017-01408) and VR (2021-02163 and 2019-03954). This work is also supported by the Program for Key Laboratory at the University of Yunnan Province, the High-level Talents Program of Yunnan University, the Yunnan Fundamental Research Projects, the “Xingdian” Talent Projects of Yunnan Province–Special Project for Young Talent, and the Chinese Jiangsu Collaborative Innovation Center for Climate Change. The authors declare no competing interests.

Data availability statement. The data that support the findings of this study are openly available at <https://esgf-node.llnl.gov/projects/cmip6/>.

REFERENCES

- Aadhar, S., and V. Mishra, 2020: On the projected decline in droughts over South Asia in CMIP6 multimodel ensemble. *J. Geophys. Res. Atmos.*, **125**, e2020JD033587, <https://doi.org/10.1029/2020JD033587>.
- Accadia, C., S. Mariani, M. Casaioli, A. Lavagnini, and A. Speranza, 2003: Sensitivity of precipitation forecast skill scores to bilinear interpolation and a simple nearest-neighbor average on high-resolution verification grids. *Wea. Forecasting*, **18**, 918–932, [https://doi.org/10.1175/1520-0434\(2003\)018<0918:SOPFSS>2.0.CO;2](https://doi.org/10.1175/1520-0434(2003)018<0918:SOPFSS>2.0.CO;2).
- Akinsanola, A. A., and K. O. Ogunjobi, 2017: Recent homogeneity analysis and long-term spatiotemporal rainfall trends in Nigeria. *Theor. Appl. Climatol.*, **128**, 275–289, <https://doi.org/10.1007/s00704-015-1701-x>.
- , G. J. Kooperman, K. A. Reed, A. G. Pendergrass, and W. M. Hannah, 2020: Projected changes in seasonal precipitation extremes over the United States in CMIP6 simulations. *Environ. Res. Lett.*, **15**, 104078, <https://doi.org/10.1088/1748-9326/abb397>.
- , K. O. Ogunjobi, A. T. Abolude, and S. Salack, 2021: Projected changes in wind speed and wind energy potential over West Africa in CMIP6 models. *Environ. Res. Lett.*, **16**, 044033, <https://doi.org/10.1088/1748-9326/abed7a>.
- Alexandersson, H., 1986: A homogeneity test applied precipitation data. *Int. J. Climatol.*, **6**, 661–675, <https://doi.org/10.1002/joc.3370060607>.
- Azorin-Molina, C., J.-A. Guijarro, T. M. McVicar, S. M. Vicente-Serrano, D. Chen, S. Jerez, and F. Espírito-Santo, 2016: Trends of daily peak wind gusts in Spain and Portugal, 1961–2014. *J. Geophys. Res. Atmos.*, **121**, 1059–1078, <https://doi.org/10.1002/2015JD024485>.
- , J. Asin, T. R. McVicar, L. Minola, J. I. Moreno-Lopez, S. M. Vicente-Serrano, and D. Chen, 2018: Evaluating anemometer drift: A statistical approach to correct biases in wind speed measurement. *Atmos. Res.*, **203**, 175–188, <https://doi.org/10.1016/j.atmosres.2017.12.010>.
- , and Coauthors, 2021: A decline of observed daily peak wind gusts with distinct seasonality in Australia, 1941–2016. *J. Climate*, **34**, 3103–3127, <https://doi.org/10.1175/JCLI-D-20-0590.1>.
- Bai, H., D. Xiao, B. Wang, D. L. Liu, P. Feng, and J. Tang, 2020: Multi-model ensemble of CMIP6 projections for future extreme climate stress on wheat in the North China Plain. *Int. J. Climatol.*, **41**, E117–E186, <https://doi.org/10.1002/joc.6674>.
- Brönnimann, S., O. Martius, H. von Waldow, C. Welker, J. Luterbacher, G. P. Compo, P. D. Sardeshmukh, and T. Usbeck, 2012: Extreme winds at northern mid-latitudes since 1871. *Meteor. Z.*, **21**, 13–27, <https://doi.org/10.1127/0941-2948/2012/0337>.
- Chen, H., J. Sun, W. Lin, and H. Xu, 2020: Comparison of CMIP6 and CMIP5 models in simulating climate extremes. *Sci. Bull.*, **65**, 1415–1418, <https://doi.org/10.1016/j.scib.2020.05.015>.
- Chen, L., S. C. Pryor, and D. Li, 2012: Assessing the performance of Intergovernmental Panel on Climate Change AR5 climate models in simulating and projecting wind speeds over China. *J. Geophys. Res.*, **117**, D24102, <https://doi.org/10.1029/2012JD017533>.
- Chen, Z., T. Zhou, L. Zhang, X. Chen, W. Zhang, and J. Jiang, 2020: Global land monsoon precipitation changes in CMIP6 precipitation. *Geophys. Res. Lett.*, **47**, e2019GL086902, <https://doi.org/10.1029/2019GL086902>.
- CMA, 2003: *Ground Surface Meteorological Observation* (in Chinese). China Meteorological Press, 157 pp.
- Cook, B. I., J. S. Mankin, K. Marvel, A. P. Williams, J. E. Smerdon, and K. J. Anchukaitis, 2020: Twenty-first century drought projections in the CMIP6 forcing scenarios. *Earth's Future*, **8**, e2019EF001461, <https://doi.org/10.1029/2019EF001461>.
- Costoya, X., A. Rocha, and D. Carvalho, 2020: Using bias-correction to improve future projections of offshore wind energy resource: A case study on the Iberian Peninsula. *Appl. Energy*, **262**, 114562, <https://doi.org/10.1016/j.apenergy.2020.114562>.
- Dadaser-Celik, F., and E. Cengiz, 2014: Wind speed trends over Turkey from 1975–2006. *Int. J. Climatol.*, **34**, 1913–1927, <https://doi.org/10.1002/joc.3810>.
- Deng, K. Q., C. Azorin-Molina, L. Minola, G. Zhang, and D. Chen, 2021: Global near-surface wind speed changes over the last decades revealed by reanalyses and CMIP6 model simulations. *J. Climate*, **34**, 2219–2234, <https://doi.org/10.1175/JCLI-D-20-0310.1>.
- Deser, C., A. S. Phillips, V. Bourdette, and H. Teng, 2012: Uncertainty in climate change projections: The role of internal variability. *Climate Dyn.*, **38**, 527–546, <https://doi.org/10.1007/s00382-010-0977-x>.
- , and Coauthors, 2020: Insights from Earth system model initial-condition large ensembles and future prospects. *Nat. Climate Change*, **10**, 791, <https://doi.org/10.1038/s41558-020-0854-5>.
- Dong, X., C. Qiu, J. Li, and H. Liu, 2018: Spatial and temporal distribution of terrestrial annual maximum wind speed in Shandong from 1981–2016 (in Chinese). *J. Mar. Meteor.*, **38**, 87–95, <https://doi.org/10.19513/j.cnki.issn2096-3599.2018.02.011>.
- Eyring, V., S. Bony, G. A. Meehl, C. A. Senior, B. Stevens, R. J. Stouffer, and K. E. Taylor, 2016: Overview of the Coupled Model Intercomparison Project phase 6 (CMIP6) experimental

- design and organization. *Geosci. Model Dev.*, **9**, 1937–1958, <https://doi.org/10.5194/gmd-9-1937-2016>.
- , and Coauthors, 2019: Taking climate model evaluation to the next level. *Nat. Climate Change*, **9**, 102–110, <https://doi.org/10.1038/s41558-018-0355-y>.
- Grose, M. R., and Coauthors, 2020: Insights from CMIP6 for Australia's future climate. *Earth's Future*, **8**, e2019EF001469, <https://doi.org/10.1029/2019EF001469>.
- Guo, H., M. Xu, and Q. Hu, 2011: Changes in near-surface wind speed in China: 1969–2005. *Int. J. Climatol.*, **31**, 349–358, <https://doi.org/10.1002/joc.2091>.
- He, B., Q. Bao, J. Li, G. Wu, Y. Liu, X. Wang, and Z. Sun, 2013: Influences of external forcing changes on the summer cooling trend over East Asia. *Climatic Change*, **117**, 829–841, <https://doi.org/10.1007/s10584-012-0592-4>.
- He, D. Y., H. Tian, and W. T. Deng, 2012: Comparative analysis of the effects of different methods in homogeneity test on annual wind speed (in Chinese). *Trans. Atmos. Sci.*, **35**, 342–349.
- Hewston, R., and S. R. Dorling, 2011: An analysis of observed daily maximum wind gusts in the UK. *J. Wind Eng. Ind. Aerodyn.*, **99**, 845–856, <https://doi.org/10.1016/j.jweia.2011.06.004>.
- IPCC, 2021: Summary for policymakers. *Climate Change 2021: The Physical Science Basis*, V. Masson-Delmotte et al., Eds., Cambridge University Press, 3–32.
- Jian, B., J. Li, Y. Zhao, Y. He, J. Wang, and J. Huang, 2020: Evaluation of the CMIP6 planetary albedo climatology using satellite observations. *Climate Dyn.*, **54**, 5145–5161, <https://doi.org/10.1007/s00382-020-05277-4>.
- Jiang, J., T. J. Zhou, X. L. Chen, and L. X. Zhang, 2020: Future changes in precipitation over Central Asia based on CMIP6 projections. *Environ. Res. Lett.*, **15**, 054009, <https://doi.org/10.1088/1748-9326/ab7d03>.
- Jiang, Y., Y. Luo, Z. Zhao, and S. Tao, 2010: Changes in wind speed over China during 1956–2004. *Theor. Appl. Climatol.*, **99**, 421, <https://doi.org/10.1007/s00704-009-0152-7>.
- , —, and —, 2013: Maximum wind speed changes over China. *Acta Meteor. Sin.*, **27**, 63–74, <https://doi.org/10.1007/s13351-013-0107-x>.
- , X. Xu, H. Liu, X. Dong, W. Wang, and G. Jia, 2017: The underestimated magnitude and decline trend in near-surface wind over China. *Atmos. Sci. Lett.*, **18**, 475–483, <https://doi.org/10.1002/asl.791>.
- , —, —, W. Wang, and X. Dong, 2018: Projection of surface wind by CMIP5 and CMIP3 in China in the 21st century (in Chinese). *J. Meteor. Environ.*, **34**, 56–63.
- Karnauskas, K. B., J. K. Lundquist, and L. Zhang, 2018: Southward shift of the global wind energy resource under high carbon dioxide emissions. *Nat. Geosci.*, **11**, 38–43, <https://doi.org/10.1038/s41561-017-0029-9>.
- Kim, J. C., and K. Paik, 2015: Recent recovery of surface wind speed after decadal decrease: A focus on South Korea. *Climate Dyn.*, **45**, 1699–1712, <https://doi.org/10.1007/s00382-015-2546-9>.
- Klink, K., 1999: Trends in mean monthly maximum and minimum surface wind speeds in the coterminous United States, 1961 to 1990. *Climate Res.*, **13**, 193–205, <https://doi.org/10.3354/cr013193>.
- Kumar, D., V. Mishra, and A. R. Ganguly, 2015: Evaluating wind extremes in CMIP5 climate models. *Climate Dyn.*, **45**, 441–453, <https://doi.org/10.1007/s00382-014-2306-2>.
- Laapas, M., and V. Venalainen, 2018: Homogenization and trend analysis of monthly mean and maximum wind speed time series in Finland, 1959–2015. *Int. J. Climatol.*, **37**, 4803–4813, <https://doi.org/10.1002/joc.5124>.
- Li, Q. X., X. N. Liu, H. Z. Zhang, and Q. P. Tu, 2003: Homogeneity study of situ observational climate series (in Chinese). *Meteor. Sci. Technol.*, **31**, 3–10.
- Li, Y., Y. Chen, Z. Li, and G. Fang, 2018: Recent recovery of surface wind speed in northwest China. *Int. J. Climatol.*, **38**, 4445–4458, <https://doi.org/10.1002/joc.5679>.
- Liu, X., X.-J. Zhang, Q. Tang, and X.-Z. Zhang, 2014: Effects of surface wind speed decline on modeled hydrological conditions in China. *Hydrol. Earth Syst. Sci.*, **18**, 2803–2813, <https://doi.org/10.5194/hess-18-2803-2014>.
- Malloy, J. W., and Coauthors, 2015: A surface wind extremes (“wind hulls” and “wind blows”) climatology for central North America and adjoining oceans (1979–2012). *J. Appl. Meteor. Climatol.*, **54**, 643–657, <https://doi.org/10.1175/JAMC-D-14-0009.1>.
- Mastylo, M., 2013: Bilinear interpolation theorems and applications. *J. Funct. Anal.*, **265**, 185–207, <https://doi.org/10.1016/j.jfa.2013.05.001>.
- McVicar, T. R., T. G. Van Niel, L. T. Li, M. L. Roderick, D. P. Rayner, L. Ricciardulli, and R. J. Donohue, 2008: Wind speed climatology and trends for Australia, 1975–2006: Capturing the stilling phenomenon and comparison with near-surface reanalysis output. *Geophys. Res. Lett.*, **35**, L20403, <https://doi.org/10.1029/2008GL035627>.
- , and Coauthors, 2012: Global review and synthesis of trends in observed terrestrial near-surface wind speeds: Implications for evaporation. *J. Hydrol.*, **416–417**, 182–205, <https://doi.org/10.1016/j.jhydrol.2011.10.024>.
- Miao, C., L. Su, Q. Sun, and Q. Duan, 2016: A nonstationary bias-correction technique to remove bias in GCM simulations. *J. Geophys. Res. Atmos.*, **121**, 5718–5735, <https://doi.org/10.1002/2015JD024159>.
- Monerie, P.-A., E. Sanchez-Gomez, B. Pohl, J. Robson, and B. W. Dong, 2017: Impact of internal variability on projections of Sahel precipitation change. *Environ. Res. Lett.*, **12**, 114003, <https://doi.org/10.1088/1748-9326/aa8cd4>.
- O'Neill, B. C., and Coauthors, 2016: The Scenario Model Intercomparison Project (ScenarioMIP) for CMIP6. *Geosci. Model Dev.*, **9**, 3461–3482, <https://doi.org/10.5194/gmd-9-3461-2016>.
- Parding, K. M., and Coauthors, 2020: GCMeval—An interactive tool for evaluation and selection of climate model ensembles. *Climate Serv.*, **18**, 100167, <https://doi.org/10.1016/j.ciser.2020.100167>.
- Peng, D. D., T. J. Zhou, L. X. Zhang, W. X. Zhang, and X. L. Chen, 2020: Observationally constrained projection of the reduced intensification of extreme climate events in Central Asia from 0.5°C less global warming. *Climate Dyn.*, **54**, 543–560, <https://doi.org/10.1007/s00382-019-05014-6>.
- Pryor, S. C., R. J. Barthelmie, N. E. Clausen, M. Drews, N. Mackellar, and E. Kjellstrom, 2012: Analyses of possible changes in intense and extreme wind speeds over Northern Europe under climate change scenarios. *Climate Dyn.*, **38**, 189–208, <https://doi.org/10.1007/s00382-010-0955-3>.
- , —, M. S. Bukovsky, L. R. Leung, and K. Sakaguchi, 2020: Climate change impacts on wind power generation. *Nat. Rev. Earth Environ.*, **1**, 627–643, <https://doi.org/10.1038/s43017-020-0101-7>.
- Shen, C., J. Zha, J. Wu, and D. Zhao, 2021a: Centennial-scale variability of terrestrial near-surface wind speed over China from reanalysis. *J. Climate*, **34**, 5829–5846, <https://doi.org/10.1175/JCLI-D-20-0436.1>.

- , —, D. Zhao, J. Wu, W. Fan, M. Yang, and Z. Li, 2021b: Estimating centennial-scale changes in global terrestrial near-surface wind speed based on CMIP6 GCMs. *Environ. Res. Lett.*, **16**, 084039, <https://doi.org/10.1088/1748-9326/ac1378>.
- Sherman, P., S. Song, X. Chen, and M. McElroy, 2021: Projected changes in wind power potential over China and India in high resolution climate models. *Environ. Res. Lett.*, **16**, 034057, <https://doi.org/10.1088/1748-9326/abe57c>.
- Song, P., and T. Zhou, 2014: The climatology and interannual variability of East Asian summer monsoon in CMIP5 coupled models: Does air-sea coupling improve the simulations. *J. Climate*, **27**, 8761–8777, <https://doi.org/10.1175/JCLI-D-14-00396.1>.
- Tian, Q., G. Huang, K. Hu, and D. Niyogi, 2019: Observed and global climate model-based changes in wind power potential over the Northern Hemisphere during 1979–2016. *Energy*, **167**, 1224–1235, <https://doi.org/10.1016/j.energy.2018.11.027>.
- Torralba, V., F. J. Doblas-Reyes, and N. Gonzalez-Reviriego, 2017: Uncertainty in recent near-surface wind speed trends: A global reanalysis intercomparison. *Environ. Res. Lett.*, **12**, 114019, <https://doi.org/10.1088/1748-9326/aa8a58>.
- Vautard, R., J. Cattiaux, P. Yiou, J.-N. Thepaut, and P. Ciais, 2010: Northern Hemisphere atmospheric stilling partly attributed to an increase in surface roughness. *Nat. Geosci.*, **3**, 756–761, <https://doi.org/10.1038/ngeo979>.
- Vose, R. S., and Coauthors, 2014: Monitoring and understanding changes in extremes: Extratropical storms, winds, and waves. *Bull. Amer. Meteor. Soc.*, **95**, 377–386, <https://doi.org/10.1175/BAMS-D-12-00162.1>.
- Wan, H., X. L. Wang, and V. R. Swail, 2010: Homogenization and trend analysis of Canadian near-surface wind speeds. *J. Climate*, **23**, 1209–1225, <https://doi.org/10.1175/2009JCLI3200.1>.
- Wang, B., and Y. Wang, 1996: Temporal structure of the Southern Oscillation as revealed by waveform and wavelet analysis. *J. Climate*, **9**, 1586–1598, [https://doi.org/10.1175/1520-0442\(1996\)009<1586:TSOTSO>2.0.CO;2](https://doi.org/10.1175/1520-0442(1996)009<1586:TSOTSO>2.0.CO;2).
- , C. Jin, and J. Liu, 2020: Understanding future change of global monsoons projected by CMIP6 models. *J. Climate*, **33**, 6471–6489, <https://doi.org/10.1175/JCLI-D-19-0993.1>.
- Wang, M., and Coauthors, 2019: Recent recovery of the boreal spring sensible heating over the Tibetan Plateau will continue in CMIP6 future projections. *Environ. Res. Lett.*, **14**, 124066, <https://doi.org/10.1088/1748-9326/ab57a3>.
- Wang, R., and Coauthors, 2017: Variation of strong dust storm events in Northern China during 1978–2007. *Atmos. Res.*, **183**, 166–172, <https://doi.org/10.1016/j.atmosres.2016.09.002>.
- Wang, X. L., 2008: Accounting for autocorrelation in detecting mean-shifts in climate data series using the penalized maximal t or F test. *J. Appl. Meteor. Climatol.*, **47**, 2423–2444, <https://doi.org/10.1175/2008JAMC1741.1>.
- , Q. H. Wen, and Y. Wu, 2007: Penalized maximal t test for detecting undocumented mean change in climate data series. *J. Appl. Meteor. Climatol.*, **46**, 916–931, <https://doi.org/10.1175/JAM2504.1>.
- Wu, J., J. Zha, and D. Zhao, 2016: Estimating the impact of the changes in land use and cover on the surface wind speed over the East China Plain during the period 1980–2011. *Climate Dyn.*, **46**, 847–863, <https://doi.org/10.1007/s00382-015-2616-z>.
- Wu, Jian, J. Zha, and D. Zhao, 2017: Evaluating the effects of land use and cover change on the decrease of surface wind speed over China in recent 30 years using a statistical downscaling method. *Climate Dyn.*, **48**, 131–149, <https://doi.org/10.1007/s00382-016-3065-z>.
- , —, —, and Q. Yang, 2018a: Changes in terrestrial near-surface wind speed and their possible causes: An overview. *Climate Dyn.*, **51**, 2039–2078, <https://doi.org/10.1007/s00382-017-3997-y>.
- , —, —, and —, 2018b: Changes of wind speed at different heights over eastern China during 1980–2011. *Int. J. Climatol.*, **38**, 4476–4495, <https://doi.org/10.1002/joc.5681>.
- Wu, J.-M., J.-S. Sun, G.-L. Sui, S.-H. Xie, and M. Wang, 2012: The change in the maximum wind speed and the impact of it on agricultural production. *Asian Agric. Res.*, **4**, 66–68, <https://doi.org/10.22004/ag.econ.142938>.
- Wu, J., Y. Shi, and Y. Xu, 2020: Evaluation and projection of surface wind speed over China based on CMIP6 GCMs. *J. Geophys. Res. Atmos.*, **125**, e2020JD033611, <https://doi.org/10.1029/2020JD033611>.
- Xu, M., C.-P. Chang, C. Fu, Y. Qi, A. Robock, D. Robinson, and H. Zhang, 2006: Steady decline of East Asian monsoon winds, 1969–2000: Evidence from direct ground measurements of wind speed. *J. Geophys. Res.*, **111**, D24111, <https://doi.org/10.1029/2006JD007337>.
- Yan, Z., S. Bate, R. E. Chandler, V. Isham, and H. Wheater, 2006: Changes in extreme wind speeds in NW Europe simulated by generalized linear models. *Theor. Appl. Climatol.*, **83**, 121–137, <https://doi.org/10.1007/s00704-005-0156-x>.
- Yan, Z. D., L. Pang, and S. Dong, 2020: Analysis of extreme wind speed estimates in the northern South China Sea. *J. Appl. Meteor. Climatol.*, **59**, 1625–1635, <https://doi.org/10.1175/JAMC-D-20-0046.1>.
- Yan, Z. W., S. Bate, R. E. Chandler, V. Isham, and H. Wheater, 2002: An analysis of daily maximum wind speed in northwest Europe using generalized linear models. *J. Climate*, **15**, 2073–2088, [https://doi.org/10.1175/1520-0442\(2002\)015<2073:AAODMW>2.0.CO;2](https://doi.org/10.1175/1520-0442(2002)015<2073:AAODMW>2.0.CO;2).
- Yu, B., G. Li, S. Chen, and H. Lin, 2020: The role of internal variability in climate change projections of North American surface temperature and temperature extremes in CanESM2 large ensemble simulations. *Climate Dyn.*, **55**, 869–885, <https://doi.org/10.1007/s00382-020-05296-1>.
- Zeng, Z., and Coauthors, 2019: A reversal in global terrestrial stilling and its implications for wind energy production. *Nat. Climate Change*, **9**, 979–985, <https://doi.org/10.1038/s41558-019-0622-6>.
- Zha, J., J. Wu, D. Zhao, and Q. Yang, 2017a: Changes of the probabilities in different ranges of near-surface wind speed in China during the period for 1970–2011. *J. Wind Eng. Ind. Aerodyn.*, **169**, 156–167, <https://doi.org/10.1016/j.jweia.2017.07.019>.
- , —, and —, 2017b: Effects of land use and cover change on the near-surface wind speed over China in the last 30 years. *Prog. Phys. Geogr.*, **41**, 46–67, <https://doi.org/10.1177/0309133316663097>.
- , D. Zhao, J. Wu, and P. Zhang, 2019: Numerical simulation of the effects of land use and cover change on the near-surface wind speed over eastern China. *Climate Dyn.*, **53**, 1783–1803, <https://doi.org/10.1007/s00382-019-04737-w>.
- , J. Wu, D. Zhao, and W. Fan, 2020: Future projections of the near-surface wind speed over eastern China based on CMIP5 datasets. *Climate Dyn.*, **54**, 2361–2385, <https://doi.org/10.1007/s00382-020-05118-4>.
- , C. Shen, D. Zhao, J. Wu, and W. Fan, 2021a: Slowdown and reversal of terrestrial near-surface wind speed and its

- future changes over eastern China. *Environ. Res. Lett.*, **16**, 034028, <https://doi.org/10.1088/1748-9326/abe2cd>.
- , D. Zhao, J. Wu, and C. Shen, 2021b: Terrestrial near-surface wind speed variations in China: Research progress and prospects. *J. Meteor. Res.*, **35**, 537–556, <https://doi.org/10.1007/s13351-021-0143-x>.
- , and Coauthors, 2021c: Projected changes in global terrestrial near-surface wind speed in 1.5°C–4.0°C global warming levels. *Environ. Res. Lett.*, **16**, 114016, <https://doi.org/10.1088/1748-9326/ac2fdd>.
- Zhang, G., C. Azorin-Molina, P. Shi, D. Lin, J. A. Guijarro, F. Kong, and D. Chen, 2019: Impact of near-surface wind speed variability on wind erosion in the eastern agro-pastoral transitional zone of Northern China, 1982–2016. *Agric. For. Meteor.*, **271**, 102–115, <https://doi.org/10.1016/j.agrformet.2019.02.039>.
- , and Coauthors, 2020: Variability of daily maximum wind speed across China, 1975–2016: An examination of likely causes. *J. Climate*, **33**, 2793–2816, <https://doi.org/10.1175/JCLI-D-19-0603.1>.
- , and Coauthors, 2021: Uneven warming likely contributed to declining near-surface wind speeds in northern China between 1961 and 2016. *J. Geophys. Res. Atmos.*, **126**, e2020JD033637, <https://doi.org/10.1029/2020JD033637>.
- Zhang, Y., L. Gao, L. Cao, Z. Yan, and Y. Wu, 2020: Decreasing atmospheric visibility associated with weakening winds from 1980–2017 over China. *Atmos. Environ.*, **224**, 117314, <https://doi.org/10.1016/j.atmosev.2020.117314>.
- Zhang, Z., and K. Wang, 2020: Stilling and recovery of the surface wind speed based on observation, reanalysis, and geostrophic wind theory over China from 1960 to 2017. *J. Climate*, **33**, 3989–4008, <https://doi.org/10.1175/JCLI-D-19-0281.1>.
- , —, and —, 2021: Quantifying and adjusting the impact of urbanization on the observed surface wind speed over China from 1985 to 2017. *Fundam. Res.*, **1**, 785–791, <https://doi.org/10.1016/j.fmre.2021.09.006>.
- , —, D. Chen, J. Li, and R. Dickinson, 2019: Increase in surface friction dominates the observed surface wind speed decline during 1973–2014 in the Northern Hemisphere lands. *J. Climate*, **32**, 7421–7435, <https://doi.org/10.1175/JCLI-D-18-0691.1>.
- Zhou, T., J. Lu, W. Zhang, and Z. Chen, 2020: The sources of uncertainty in the projection of global land monsoon precipitation. *Geophys. Res. Lett.*, **47**, e2020GL088415, <https://doi.org/10.1029/2020GL088415>.
- Zhu, S., F. Ge, Y. Fan, L. Zhang, F. Sielmann, K. Fraedrich, and X. Zhi, 2020: Conspicuous temperature extremes over Southeast Asia: Seasonal variations under 1.5°C and 2°C global warming. *Climatic Change*, **160**, 343–360, <https://doi.org/10.1007/s10584-019-02640-1>.